CM^2

Magazine

第 129 期

创刊词

海洋是生命的摇篮，是文明的纽带。地球上最早的生命诞生于海洋，海洋里的生命最终进化成了人类，人类的文化融合又通过海洋得以实现。人因海而兴。

人类对海洋的探索从未停止。从远古时代美丽的神话传说，到麦哲伦的全球航行，再到现代对大洋的科学钻探计划，海洋逐渐从人类敬畏崇拜幻想的精神寄托演变成可以开发利用与科学研究的客观存在。其中，上个世纪与太空探索同步发展的大洋科学钻探计划将人类对海洋的认知推向了崭新的纬度：深海（deep sea）与深时（deep time）。大洋钻探计划让人类知道，奔流不息的大海之下，埋藏的却是亿万年的地球历史。它们记录了地球板块的运动，从而使板块构造学说得到证实；它们记录了地球环境的演变，从而让古海洋学方兴未艾。

在探索海洋的悠久历史中，从大航海时代的导航，到大洋钻探计划中不可或缺的磁性地层学，磁学发挥了不可替代的作用。这不是偶然，因为从微观到宏观，磁性是最基本的物理属性之一，可以说，万物皆有磁性。基于课题组的学科背景和对海洋的理解，我们对海洋的探索以磁学为主要手段，海洋磁学中心因此而生。

海洋磁学中心，简称 CM^2，一为其全名"Centre for Marine Magnetism"的缩写，另者恰与爱因斯坦著名的质能方程 $E = MC^2$ 对称，借以表达我们对科学巨匠的敬仰和对科学的不懈追求。

然而科学从来不是单打独斗的产物。我们以磁学为研究海洋的主攻利器，但绝不仅限于磁学。凡与磁学相关的领域均是我们关注的重点。为了跟踪反映国内外地球科学特别是与磁学有关的地球科学领域的最新研究进展，海洋磁学中心特地主办 CM^2 Magazine，以期与各位地球科学工作者相互交流学习、合作共进！

"海洋孕育了生命，联通了世界，促进了发展"。21 世纪是海洋科学的时代，由陆向海，让我们携手迈进中国海洋科学的黄金时代。

目 录

1

1. 持续性海洋热浪引起海-气 CO_2 通量降低

翻译人：仲义 zhongy@sustech.edu.cn

摘要：区域性过程对于全球碳收支具有重要的调控作用。全球大洋中纬度地区吸收海洋 CO_2 可以抵消热带地区对于 CO_2 释放，同时受到海洋热浪的影响。然而，我们缺乏关于海洋热浪的持续性观测以及它们对二氧化碳敏感区的影响。本文，作者使用 1985-2017 年的重建和海洋再分析和卫星数据的联合分析表明，持续的海洋热浪发生在主要的二氧化碳吸收和释放区域。持续的海洋热浪造成平均海气 CO_2 通量密度变化在太平洋最强，且与 ENSO 相关的热带地区的 CO_2 释放减少了 $40\pm9\%$，在研究期间北太平洋的 CO_2 吸收减少了 $29\pm11\%$。这些结果为极端环境变化相互作用和关键的调节海洋生态系统服务提供了新的见解，并为未来研究其在气候变化下的演变铺平了道路。

ABSTRACT: Regional processes play a key role in the global carbon budget. Major ocean CO_2 uptake at mid-latitudes counteracts CO_2 release in the tropics, which is modulated by episodes of marine heatwaves. Yet, we lack essential knowledge on persistent marine heatwaves, and their effect on the CO2 sensitive areas. Here we show, using a 1985-2017 joint analysis of reconstructions, ocean reanalysis and in situ and satellite data, that persistent marine heat waves occur in major CO_2 uptake and release areas. Average air-sea CO_2 flux density changes from persistent marine heatwaves are strongest in the Pacific Ocean with a $40\pm9\%$ reduction in CO_2 release in the tropics linked to ENSO, and a reduction in CO_2 uptake of $29\pm11\%$ in the North Pacific over the study period. These results provide new insights into the interplay of extreme variability and a critical regulating ocean ecosystem service, and pave the way for future investigations on its evolution under climate change.
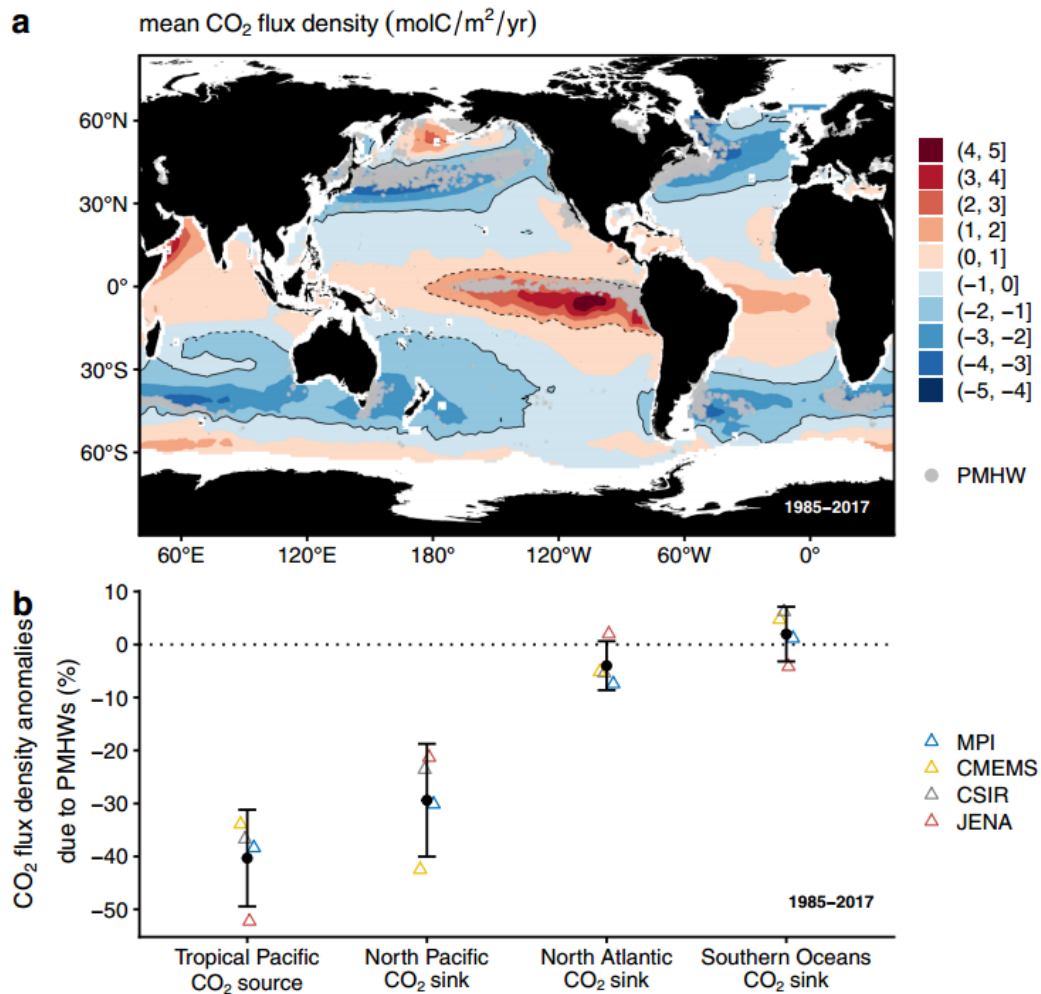
Figure 1. Interplay of PMHWs and oceanic carbon CO_2 source and sink areas. a Mean 1985–2017 air-to-sea CO_2 flux density (FCO_2) derived from the Copernicus Marine Service (CMEMS) observation-based product (see methods section). Negative values indicate oceanic uptake (blue), while positive values indicate oceanic outgassing (red) of CO_2. The black continuous/dashed contours represent critical CO_2 sink/source regions, i.e the regions where the mean 1985–2017 FCO_2 is lower/greater than $-1/1$ molC/m2/yr as proposed by Takahashi et al.[35]. The gray points represent satellite Sea Surface Temperature grid points that have experienced at least 3 PMHWs from 1985 to 2017 (see text for details). b Trimmed average percent FCO_2 anomalies during PMHWs derived from an ensemble of four observation-based products of FCO_2 (see section methods) in critical oceanic CO_2 sinks and sources (plain and dashed contours in Fig. 1a) that are impacted by PMHWs. The percent FCO_2 anomalies correspond to the monthly FCO_2 anomalies divided by the monthly FCO_2 climatological values (see section methods). Negative values corresponds to a reduction in

both a source or a sink region. The 95% confidence interval for each trimmed average percent FCO_2 anomalies are indicated in the Supplementary Table 1. We verified that all trimmed average percent FCO_2 anomalies were significantly different from 0 using a Yuen's trimmed mean test. The ensemble mean and standard deviation are given in black. An additional 12% uncertainty resulting from uncertain gas exchange has been added to the ensemble spread. The calculation of the percent FCO_2 anomalies is detailed in the method section.

MECHANIMS LEADING TO A REDUCTION IN THE AIR-SEA CO₂ FLUX DENSITY IN THE PACIFIC DURING PERSISTENT MARINE HEATWAVES
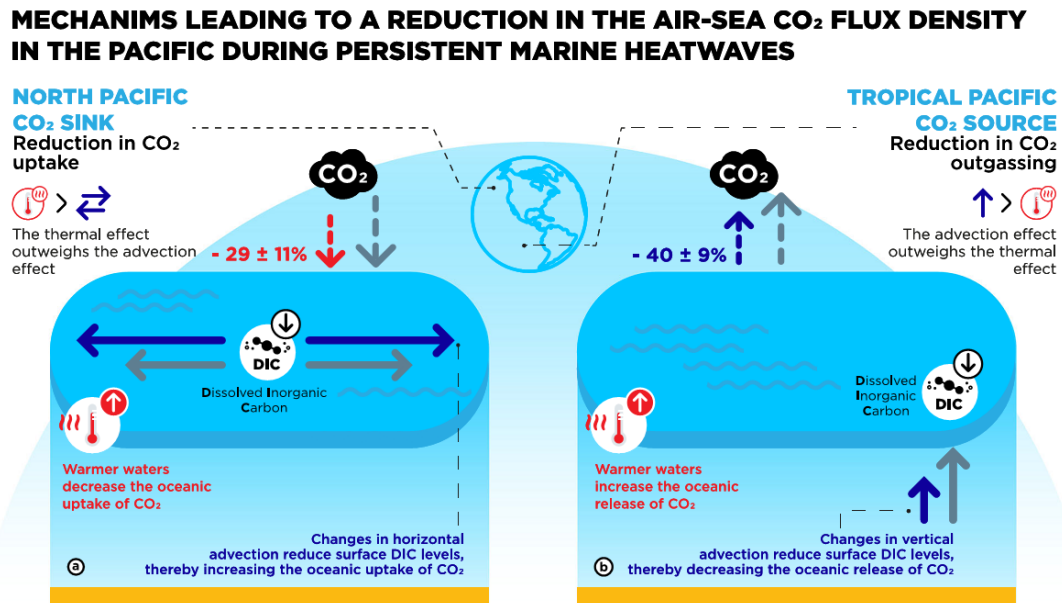
Figure 2. Schematic presentation of the mechanisms driving the reduction in the air-sea CO_2 flux density in (a) the North Pacific CO_2 sink and (b) the Tropical Pacific CO_2 source regions. Red color indicates the thermal effect on the air-sea CO_2 flux density, the blue color is linked to impacts related to circulations changes associated with PMHWs such as anomalous horizontal and vertical advection. The gray color represents the normal conditions. See text for more details.

2. 副特提斯洋海道（塔里木盆地，中国西部）的钙质浮游生物对古新世-始新世极热事件的响应

翻译人：张靖宇 zhangjy6@sustech.edu.cn

摘要： 古新世-始新世极热事件（PETM）是发生在 56 百万年前的一次全球快速变暖，被广泛认为与目前由人为二氧化碳排放引起的变暖类似。中国西北部塔里木盆地出露的完整、连续的古近纪浅海地层，是研究 PETM 期间副特提斯洋海道古环境变化的理想场所。到目前为止，塔里木盆地的 PETM 区间还没有进行高分辨率的钙质超微化石生物地层学研究。Kuzigongsu 剖面的齐姆根组地层的野外露头样品含有丰富的、保存良好的钙质超微化石，可以建立一个高分辨率的生物地层框架。总体而言，观察到 33 个属的 73 种钙质超微化石，主要物种包括 *Coccolithus pelagicus*、各种 *Toweius* 种属、*Pontosphaera exilis* 和 *Micrantholithus flos*。五个钙质超微化石数据点可以确认 NP6 区到 NP10 区的化石。浅水类（*Micrantholithus*）在整个剖面上的共同出现，表明 Kuzigongsu 剖面的沉积环境为中-外浅海。Excursion taxa "（Coccolithus bownii, Discoaster araneus, D. acutus, Rhomboaster spp.）的地层分布与 $\delta^{13}C_{carb}$ 和 $\delta^{18}O_{carb}$ 的负偏移范围一致，表明这些 excursion taxa 是识别副特提斯洋海道中 PETM 存在的微古生物手段。在 PETM 期间，保存差、丰度极低的超微化石与 $CaCO_3$ 值接近零 wt%，表明在副特提斯洋海道的浅水区发生了海洋酸化。此外，作为高生产力指标的 *Neochiastozygus junctus* 物种明显增加，表明表层海洋生产力提高。更高的初级生产力可能是由增强的大陆风化作用引发的，通过河流径流提供更多的营养物质。

ABSTRACT: The Paleocene-Eocene Thermal Maximum (PETM) was a rapid global warming occurred 56 million years ago and has been widely viewed as an ancient analogue to the ongoing warming driven by anthropogenic CO_2 emissions. The complete and continuous Paleogene shallow marine strata well preserved and outcropped in the Tarim Basin, northwestern China are ideal to study the paleoenvironmental change of the Paratethys Seaway during the PETM. To date, no high-resolution calcareous nannofossil biostratigraphy has been performed for the PETM interval in the

Tarim Basin. Outcrop samples taken from the Qimugen Formation in the Kuzigongsu section contain abundant, moderately well preserved calcareous nannofossils allows for the establishment of a high-resolution biostratigraphic framework. Overall, 73 species of calcareous nannofossils from 33 genera were observed, with the dominant species including *Coccolithus pelagicus*, various *Toweius* species, *Pontosphaera exilis*, and *Micrantholithus flos*. The five calcareous nannofossil datums allow for the recognition of nannofossil Zone NP6 through Zone NP10. The common occurrence of shallow-water taxa (*Micrantholithus*) throughout the section suggests a middle to outer neritic setting for depositional environment of the Kuzigongsu section. The stratigraphic distribution of "excursion taxa" (*Coccolithus bownii, Discoaster araneus*, *D. acutus*, *Rhomboaster* spp.) is consistent with the range of negative excursion in $\delta^{13}C_{carb}$ and $\delta^{18}O_{carb}$, indicating that these excursion taxa are micropaleontological means for identifying the presence of the PETM in the Paratethys Seaway. During the PETM, the deteriorated preservation and extremely low abundance of nannofossils and near-zero wt% $CaCO_3$ values suggest that ocean acidification occurred in the shallow water of the Paratethys Seaway. In addition, a significant increase in the species *Neochiastozygus junctus*, which is a high productivity indicator indicates increased surface ocean productivity. Higher primary productivity may be triggered by enhanced continental weathering delivering increased nutrient through river runoff.
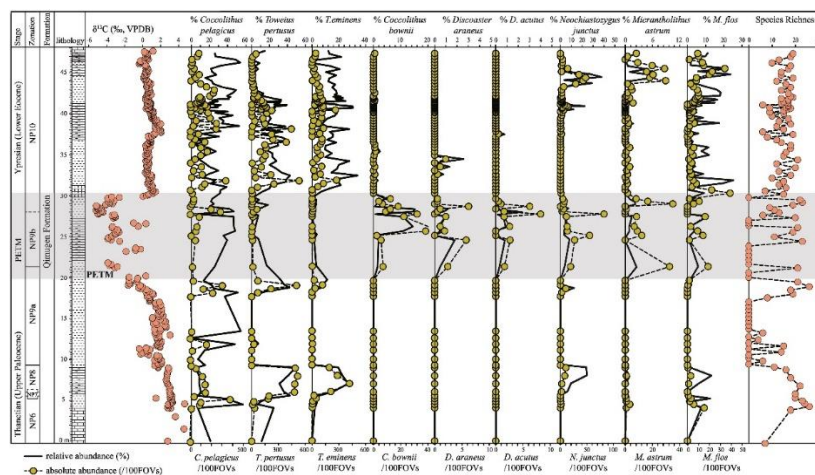
Figure 1. Variation in selected calcareous nannofossil species across the PETM at the Kuzigongsu section, Tarim Basin (NW China). Solid line denotes percentage abundance, and dashed line indicates absolute abundance (number of specimens encountered in 100 FOVs).

3. 沉积物源视角的青藏高原东部主要河流演化特征

翻译人：刘伟 inewway@163.com

摘要： 青藏高原东部主要河流的起源和演化因为与构造隆升和气候变化密切相关而一直是研究的重点。本文综述了一系列沉积物源研究,旨在约束西藏东部地区主要河流的流域演变,包括湄公河、红河、珠江、长江和黄河。湄公河的形成时间不晚于~17 Ma,可能是中新世中期东亚夏季风降水增强所致。青藏高原东南部以前认为可能存在流入宋红-莺歌海盆地的单一大的古红河,但这与宋红-莺歌海盆地的物源信号明显不符,表明晚始新世以来没有大规模的古红河沉积。珠江形成于晚渐新世,此时珠江口盆地物源发生剧烈变化。同时,中国东南沿海的河流(如闽江)也向西迁移。这些线索表明,中国东南部的古河流在晚渐新世开始向内陆迁移。相比之下,长江的形成时间一直争论不休,从晚白垩世到全新世,主要是由于这条跨大陆河流复杂的演化史。长江第一弯的形成可能发生在始新世晚期,是由局部岩浆活动和/或哀老山-红河断裂运动引起的区域地形梯度变化所致。陆上和海上物源证据表明,三峡的贯通时间不晚于中新世晚期。黄河方弯的形成早于上新世晚期,而连接黄河上中下游的关键切入点三门峡的贯通时间则可能出现在早更新世(~1.2 Ma)。在历史悠久、连续的沉积记录上,多物源指标可以为西藏东部主要河流的起源与演化提供客观信息。尽管这些河流的演变历史仍有争议,但河流演变、气候和构造事件的比较表明,始新世局部的和孤立的流域模式可能与东亚的干旱气候条件有关。渐新世和晚中新世河流向内陆伸展与东亚季风的形成和青藏高原生长、东亚边缘盆地裂陷等重大构造事件发生的时间重合,凸显了气候和构造对河流演化的控制作用。

ABSTRACT: The origin and development of the major rivers in the eastern Tibetan Plateau have been a special focus of research because of the close links recognized between river formation, tectonic uplift, and climate change. In this article, we review a number of sedimentary provenance investigations aiming to constrain the drainage evolution of the main rivers draining eastern Tibet, including the Mekong, Red, Pearl, Yangtze, and Yellow rivers. The Mekong River was formed no

later than ~17 Ma, likely triggered by a period of enhanced East Asian summer monsoon precipitation during the middle Miocene. A single large paleo-Red River draining the southeastern Tibetan Plateau into the Song Hong - Yinggehai Basin had been proposed to explain the unusual drainage pattern. However, this is not compatible with the distinctive provenance signals in the southeastern Tibetan river sands compared with the Song Hong - Yinggehai Basin, indicating that there has been no large-scale paleo-Red River since the late Eocene. The Pearl River has formed during the late Oligocene, as there was a sharp provenance change in the Pearl River Mouth Basin. Moreover, rivers draining southeast coastal China (e.g., Min River) migrated westward at the same time. These clues highlight that paleo-rivers in southeastern China started to migrate inland during the Late Oligocene. In contrast, the formation timing of the Yangtze River is still under intensively debated, ranging from late Cretaceous to Holocene, mainly due to the complex evolution history of this trans-continental river. The formation of the First Bend of the Yangtze River likely happened during the late Eocene, resulting from changes in the regional topographic gradient triggered by local magmatic activity and/or movement of the Ailao Shan-Red River Fault. Onshore and offshore provenance evidence indicate that incision of the Three Gorges happened no later than the late Miocene. Formation of the Square Bend of the Yellow River occurred prior to the late Pliocene, while incision of the Sanmen Gorge, a key capture point connecting the upper-middle and lower Yellow River likely occurred in the early Pleistocene (~1.2 Ma). Multi-provenance proxies on well-dated and continuous sedimentary records can provide objective information in terms of the origin and evolution of the major rivers flowing from eastern Tibet. Although the evolution of these rivers remains debatable, a comparison among the river evolution, climatic and tectonic events suggests that Eocene local and isolated drainage patterns is likely related to the dry climate condition in the East Asia. Oligocene and late Miocene inlandward expansion and integration of rivers coincides with both the formation of the East Asian Monsoon and the timing of major tectonic events, such as the growth of the Tibetan Plateau and the rifting and opening of the eastern Asian marginal basins, highlighting the importance of climate and tectonics in controlling the evolution of major rivers.
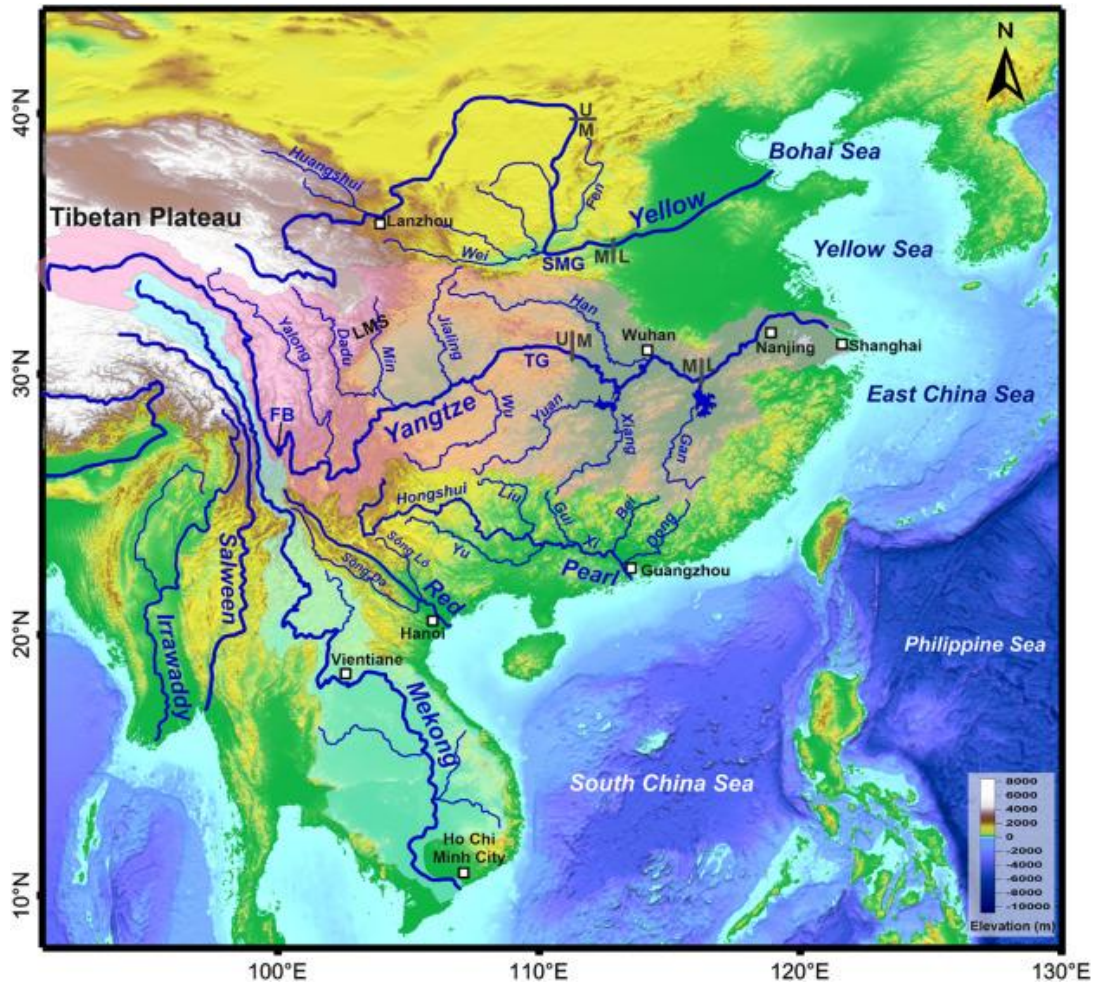
Figure 1. Sketch map showing the major fluvial systems draining eastern Asia and their major tributaries. The Yangtze and Yellow Rivers are divided into the upper (U), middle (M) and lower (L) reaches by grey lines. The pink and blue areas represent the Yangtze and Mekong drainage areas, respectively. LMS = Longmenshan; FB = First Bend; TG = Three Gorges; SMG = Sanmen Gorges. (For interpretation of the references to colour in this figure legend, the reader is referred to the web version of this article.)

4. 石笋生长层中磁性矿物颗粒的存在与分布规律

翻译人：杨会会 11849590@mail.sustech.edu.cn

摘要：石笋中磁性颗粒的浓度与区域水文条件密切相关，可作为古气候重建的重要指标。这种磁学研究通常选择石笋的中轴区域。然而，外源性磁性矿物颗粒在生长层内的分布及其影响因素尚不清楚。本文采用等温剩磁获得曲线和低温磁分析等方法，研究了三种形状石笋生长纹层中磁性颗粒的赋存状态和变化规律。结果表明:剩磁载体以碎屑磁铁矿/磁赤铁矿为主，同时存在少量赤铁矿和针铁矿;三种形状的石笋(圆顶状、圆锥形、蜡烛状)生长纹上的软磁颗粒分布呈现不同的规律。对于圆顶形石笋，各生长层的软磁颗粒浓度从中心到边缘呈增加趋势。类似的模式也出现在圆锥形和蜡烛状石笋的底部生长层中。这种磁性颗粒的边缘富集是由滴水的水洗作用（washing effect）引起的。但在圆锥形和蜡烛状石笋的顶部生长层，这种富集模式减弱甚至相反，说明石笋的形状也会影响软磁矿物的表面分布。这些磁颗粒的不均匀分布意味着石笋的中轴区域可能并不总是环境磁学研究的最佳样本。

ABSTRACT: The concentrations of magnetic particles in stalagmites depend greatly on the regional hydrologic condition, and thus can act as an important proxy for paleoclimate reconstruction. The central axis region of a stalagmite is usually selected for such magnetism study. However, little is known about the distribution and influence factors of exogenetic magnetic particles within the growth laminae. In this study, the occurrence and variations of magnetic particles along the growth laminae of three shape stalagmites were investigated by a set of magnetic measurements, including isothermal remanent magnetization (IRM) acquisition curves and low-temperature magnetic analysis. The results show the main magnetic remanence carrier is detrital magnetite/maghemite, coexisting with small amounts of hematite and goethite. The distribution of soft magnetic particles along the growth laminae showed different patterns among the three shape

stalagmites (dome, cone, candle). For the dome shape stalagmite, the soft magnetic particle concentrations in all studied growth layers showed an increasing trend from center to edge. Similar patterns were also appeared in the bottom growth layers of the cone and candle shape stalagmites. This edge enrichment of magnetic particles is caused by drip water washing effect. However, such enrichment pattern became weaker or even inverse in the top growth layers of the cone and candle shape stalagmites, indicating that the shapes of stalagmites could also affect the surface distribution of soft magnetic minerals. These uneven distributions of magnetic particles imply that the central axis region of a stalagmite may not always be the optimal specimen for environmental magnetism study.
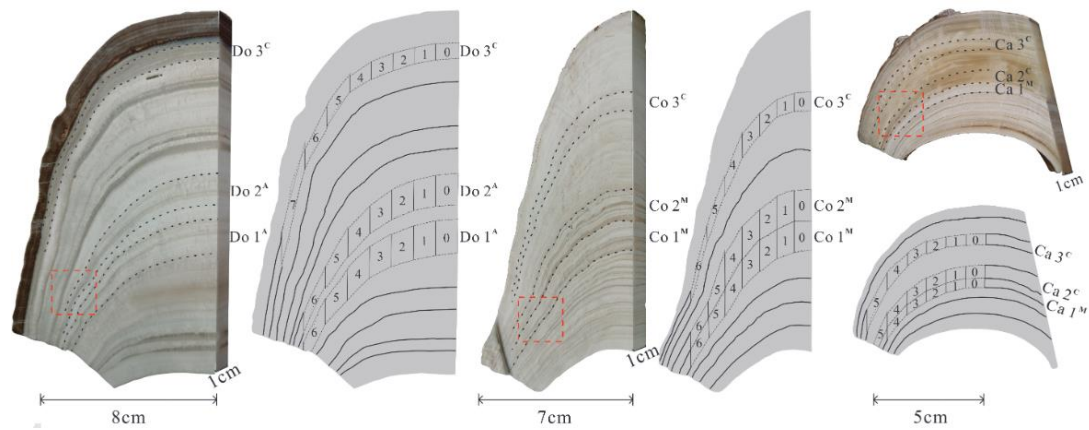
Figure 1. Sampling strategy of the three shape stalagmites(Do = dome, Co = cone shape, Ca = candle). The red dotted line in original figures indicates the position of cubic specimens behind the sheet. Do 1-3, Ca 1-3 and Co 1-3 indicate banded layers from base to top, and their superscript A, C and M on the right side represent aragonite, calcite and their mixture respectively, reflecting the main mineral composition of the corresponding binding layers. Gray solid rectangles distributed along growth laminae are cutting positions, and the number in each rectangle denotes the specimen number. Black solid line and dotted line depict growth laminae.
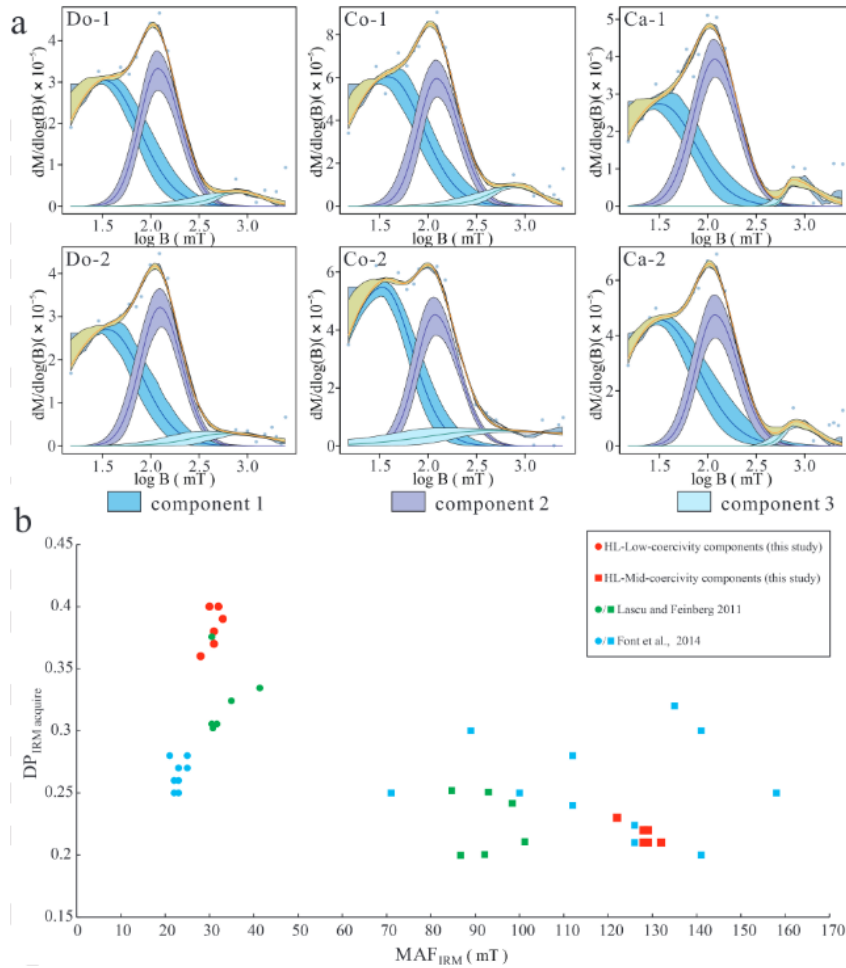
Figure 2. The magnetic coercivity distribution of six cubic specimens. Magnetic components of the specimens were identified from deconvolution of IRM acquisition gradient curves on MAX UnMix website (Maxbauer et al., 2016). (b) Plot of the MAF_{IRM} vs. $DP_{IRMacquire}$. Red circles and squares represent the low-coercivity component and the mid-coercivity component from HL cave (this study), respectively. Green circles and squares represent the detrital low-coercivity component (non-biogenic magnetite) and the mid-coercivity component (partially oxidized magnetite and maghemite) determined from deconvolution of IRM acquisition gradient curves from four stalagmites (HL-06, YX-17, QT from China, and SVC982 from Minnesota), respectively (Lascu and Feinberg, 2011).Blue circles and squares represent the detrital low-coercivity component (magnetite/maghemite) and the mid-coercivity component (hematite) determined from deconvolution of IRM acquisition gradient curves fromfresh stalagmite SPAII, Portugal (Font et al., 2014).

5. 根据季节分解的洞穴记录，北美大陆中部全新世晚期冬季降水量增加

翻译人：王浩森 11930841@mail.sustech.edu.cn

摘要： 尽管这些记录能够更好地理解驱动亚年度气候变化的潜在因素，但全新世的亚年度气候重建是罕见的。我们使用专门的共焦激光荧光显微镜成像和自动二次离子质谱微分析来解析北美大陆中部全新世晚期（2.7-2.1 ka）洞穴的季节性氧同位素（$\delta^{18}O$）记录。我们通过测量晚全新世 600 年跨度内 117 个年度带内 $\delta^{18}O$ 的变化（$\Delta^{18}O$）来实现这一点。我们解释了 2.4±0.1 ka 后 $\Delta^{18}O$ 值的变化，以反映冬季降水量的增加。我们的研究对过去的季节性进行了直接测量，为北美中部全新世晚期发生的季节性降水模式的变化提供了新的见解，并为理解该地区复杂的降水和温度历史提供了新的工具。

ABSTRACT: Subannual climate reconstructions of the Holocene are rare despite the ability of such records to provide a better understanding of the underlying factors that drive subannual climate variability. We used specialized confocal laser fluorescent microscope imaging and automated secondary ion mass spectrometry microanalysis to resolve a seasonal oxygen isotope ($\delta^{18}O$) record of a late Holocene–aged (2.7-2.1 ka) speleothem from mid-continental North America. We did this by measuring intra-band $\delta18O$ variability ($\Delta^{18}O$) within 117 annual bands over a 600 yr span of the late Holocene. We interpret a change in $\Delta^{18}O$ values after 2.4 ± 0.1 ka to reflect an increase in the amount of winter precipitation. Our study produced direct measurements of past seasonality, offers new insights into shifting seasonal precipitation patterns that occurred during the late Holocene in central North America, and adds a new tool for understanding the complex precipitation and temperature histories of this region.
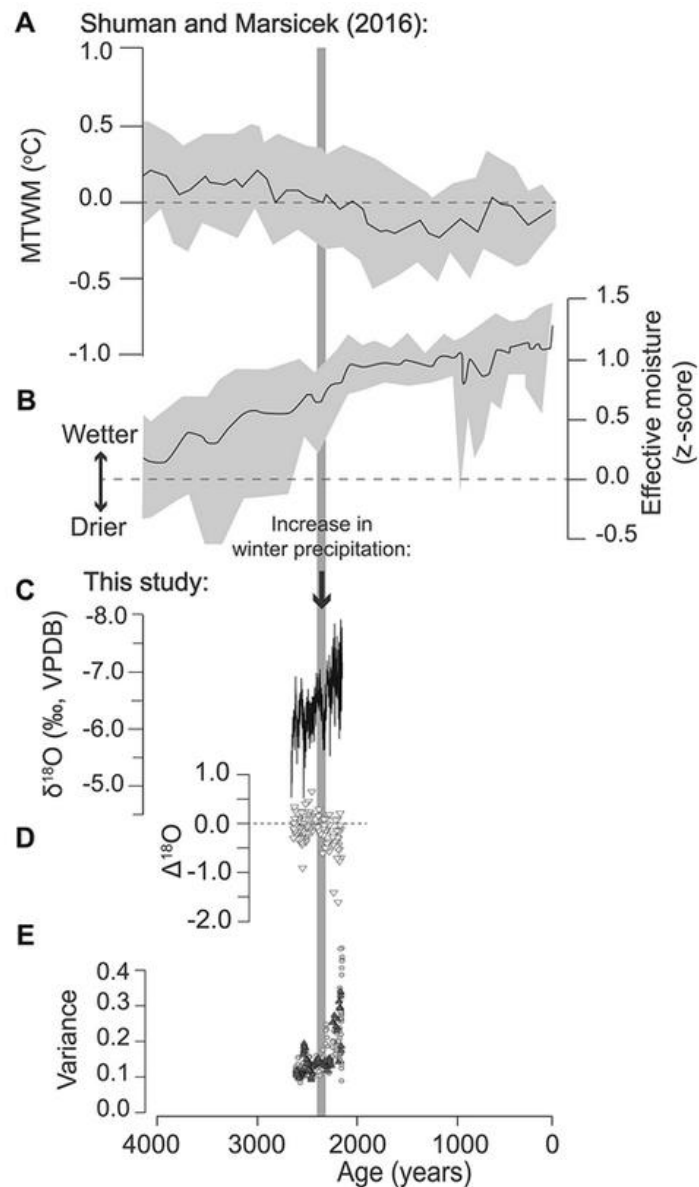
Figure 1. GStalagmite CM-4 (from the Cave of the Mounds, Wisconsin, USA) δ^{18}O record in context with regional paleoclimate records for the past 4 k.y. (A,B) Late Holocene trends in mean temperature of warmest month (MTWM) and effective moisture at several sites that span across the upper central-to-eastern United States (see Shuman and Marsicek, 2016). (C) Stalagmite CM-4 δ^{18}O record (this study) labeled with timing of the seasonal shift in moisture (ca. 2.4 ka; black arrow and vertical gray shading) as inferred from calculations of intra-band δ^{18}O variability (Δ^{18}O; panel D). (D) Intra-band δ^{18}O variability within annual bands of stalagmite CM-4 (Δ^{18}O). (E) Running-variance (every 10 data points) of δ^{18}O$_B$ (light gray) and δ^{18}O$_D$ (dark gray). Note the distinct increase in variance at ~2.4 ka. VPDB-Vienna Peedee belemnite.

6. 古气候预示在变暖的未来东亚冬季风将减弱和幅度减小

翻译人：曹伟 11930854@qq.com

摘要：东亚冬季风(EAWM)对北方冬季东亚地区的天气、气候、经济和社会有着重要的影响，对其未来的预测具有重要的科学和现实意义。然而，依靠地质 EAWM 重建来弥补仪器记录局限性的预测仍然缺乏并且迫切需要。在仪器变化和地质变化的双重背景下进行 EAWM 预测更有前景。我们利用中国黄土高原上 4 个高分辨率、年代明确的黄土剖面的粒度记录来代表过去 EAWM 强度及其振幅。结果表明，在不同的时间尺度上，暖期的 EAWM 比冷期弱且振幅更低。此外，仪器记录显示，在全球变暖的背景下，1980 年代中期以后的 EAWM 水平较弱，年际振幅减小。我们认为，在 21 世纪全球变暖情景下，EAWM 将经历长期的减弱和降低(如年际)。

ABSTRACT: The East Asian winter monsoon (EAWM) has significant impacts on the weather and climate, and subsequently on the economy and society, in East Asia during boreal winters, and its projection into the future is scientifically and practically significant. However, projections relying on geological EAWM reconstructions, which can compensate for instrumental record limitations, are still lacking and urgently needed. It is more promising to conduct prediction under the background of not only instrumental but also geological changes in the EAWM. We used grain-size records from four high-resolution, chronologically well-defined loess sections on the Chinese Loess Plateau to represent past EAWM intensity and its amplitudes. Our results show that the EAWM is weaker and has lower amplitudes during warm periods than during cold stages at various time scales. Moreover, instrumental records reveal that the EAWM shows a weak level and reduced interannual amplitudes after the mid-1980s under the context of global warming. We propose that

the EAWM will experience long-term weakening and reduced (e.g., interannual) amplitudes under 21st century global-warming scenarios.
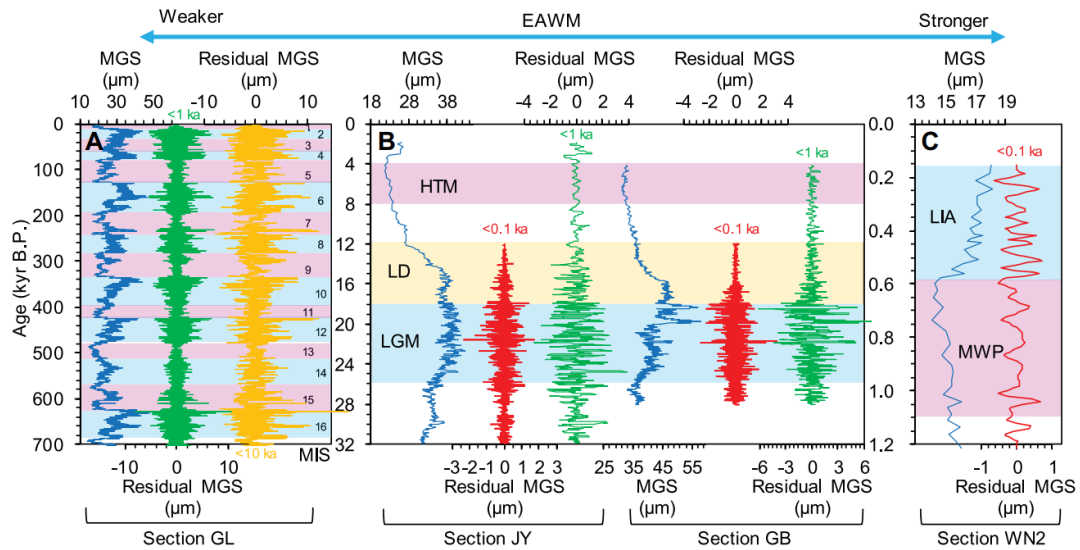
Figure 1. Multi-time-scale changes in the East Asian winter monsoon (EAWM) intensity represented by mean grain size (MGS) and residual (interpolated minus smoothed) MGS at sections GL (Gulang) (A), JY (Jingyuan) and GB (Gaobai) (B), and WN2 (Weinan) (C) on the Chinese Loess Plateau (see Fig. 1 for locations), with larger and smaller values indicating stronger and weaker EAWM, respectively. Light blue and pink bands indicate relatively cold and warm periods, respectively (MIS marine isotope stage; LGM Last Glacial Maximum; HTM Holocene Thermal Maximum; MWP Medieval Warm Period; LIA Little Ice Age), and yellow band in B marks last deglaciation (LD). Limited by resolution (Table S2 [see footnote 1]), multidecadalscale data covering Holocene at sections JY and GB were not used.

7. 早寒武世类似于埃迪卡拉纪极弱的偶极矩：地磁场长期趋势的证据？

翻译人：张伟杰 12031188@mail.sustech.edu.cn

摘要：古强度数据可以揭示地球发电机的状态，为地球深部事件提供约束条件，以及了解古磁场的长期趋势。近期研究揭示埃迪卡拉纪(635 Ma - 539 Ma)是一个持续的古地磁场强度极弱的特别时期。这个时间段也与一些最近通过数值地球发电机模型和古强度数据长期特征分析评估的地球内核成核(ICN)年龄相吻合。然而，随后的寒武纪(540 Ma - 485 Ma)由于几乎没有数据，其场强在很大程度上是未知的。本文提供了寒武纪高质量的古强度数据。Grenville岩墙(~590 Ma)经历了 Chatham-Grenville 岩株(532 Ma)烘烤，以岩株控制的降温速率缓慢冷却，记录了这段时间(可达数万年)内的平均古强度。该岩墙的古地磁特征方向与之前从 Chatham-Grenville 和 Mont Riguad 岩株中获得的方向一致。利用多种方法获得的古强度结果表明，频繁倒转的极弱地磁场延伸至晚寒武纪。磁偶极强度与埃迪卡拉纪"极弱"的磁场相似，可能表明这种古地磁行为一直持续到寒武纪。这一时间段的弱磁场的原因仍然是谜，但不排除大约 2 亿年的准周期偶极场强度变化延伸至整个显生宙。

ABSTRACT: Paleointensity data can yield insight on the state of the geodynamo, providing constraints on deep Earth events and enabling analysis of long-term trends in the paleomagnetic field. The Ediacaran (635 Ma–539 Ma) is a period of discrepant paleomagnetic behaviour that was recently characterised by sustained, extremely weak, paleointensity. The interval also coincides with some of the most recent estimates for Earth's inner core nucleation (ICN) age, determined from numerical geodynamo models and analysis of long-term paleointensity data. However, the field

strength during the subsequent Cambrian period (540 Ma–485 Ma) is largely unknown with almost no data.

Here, we provide high-quality paleointensity results for the Cambrian. A Grenville dyke (~590 Ma) that was baked by the Chatham-Grenville stock (532 Ma), slowly cooled at a rate controlled by the stock and recorded the paleointensity averaged over this interval (up to several tens of thousands of years). The characteristic paleomagnetic directions of the dyke are well-defined and consistent with those previously obtained from the Chatham-Grenville and Mont Riguad stocks.

Paleointensity data were obtained using multiple methods and indicate an extremely weak field during a period coincidental with evidence for hyper-reversing activity extending into the late Cambrian. The dipole strength is similar to that of the 'ultra-weak' Ediacaran and may suggest that this paleomagnetic behaviour persisted into the Cambrian. The cause of this weak-field interval remains enigmatic but an approximate 200-million-year quasi-periodicity in dipole strength extending across the entire Phanerozoic is not ruled out.
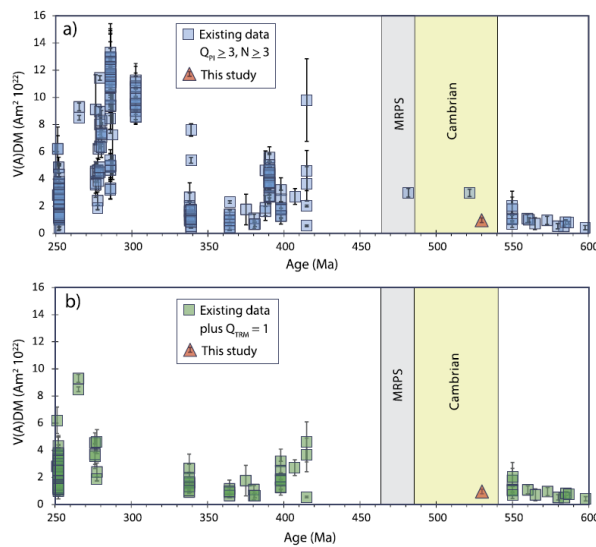
Figure 1. Virtual (Axial) Dipole moment data for the period 600-250 Ma. All data is from the latest version of the PINT database (v.8.0.0; http://www.pintdb .org/; Bono et al., 2022). Error bars denote one standard deviation. MPRS; Moyero reversed polarity superchron. a)Q_{PI}scored and filtered to only include Q_{PI}>3and N>3. b)The same data as in (a) is additional filtered to only include data that passes the Q_{TRM} criteria.

8. 减弱的 AMOC 可能会延长温室气体引起的地中海干旱

翻译人：李海 12031330@mail.sustech.edu.cn

摘要：地中海被确定为研究气候变化的热点区域,模型预测结果显示,随着温室气体的增加,该地区气候变暖和降雨量下降。降雨量减少将对农业和水资源产生影响。这些变化是否可以通过大幅减少温室气体而逆转？为探究这一点,作者研究了具有各种未来辐射强迫状态的高分辨率气候模型，包括温室气体浓度从 21 世纪中期开始大幅度减少的情景。未来应对温室气体的减少,地中海夏季雨量的下降趋势发生逆转,但冬季降雨量的下降趋势仍在继续。这种持续的冬季降雨量下降是由于地中海西部持续存在的大气反气旋造成的。进一步的数值实验表明，反气旋和持续的冬季降雨量减少可归因于温室气体引起的大西洋经向翻转流（AMOC）的减弱,这种减弱在整个 21 世纪都在持续。持续较弱的 AMOC,加上温室气体的减少,造成北大西洋副极地的快速冷却和海冰增长。这种冷却导致北大西洋副极地环流上空出现强烈的气旋性大气环流异常,并通过大气遥相关引起地中海上空的反气旋性环流异常。尽管显著缓解了气候变化,但未能扭转冬季降雨量下降的趋势,这是气候系统中"意外"的一个例子。在这种情况下,持续的 AMOC 变化出人意料地阻碍了地中海气候变化的可逆性。这些意外可能使全面恢复气候的道路复杂化。

ABSTRACT: The Mediterranean region has been identified as a climate hot spot, with models projecting a robust warming and rainfall decline in response to increasing greenhouse gases. The projected rainfall decline would have impacts on agriculture and water resources. Can such changes be reversed with significant reductions in greenhouse gases? To explore this, we examine large ensembles of a high-resolution climate model with various future radiative forcing scenarios,

including a scenario with substantial reductions in greenhouse gas concentrations beginning in the mid-21st century. In response to greenhouse gas reductions, the Mediterranean summer rainfall decline is reversed, but the winter rainfall decline continues. This continued winter rainfall decline results from a persistent atmospheric anticyclone over the western Mediterranean. Using additional numerical experiments, we show that the anticyclone and continued winter rainfall decline are attributable to greenhouse gas–induced weakening of the Atlantic Meridional Overturning Circulation (AMOC) that continues throughout the 21st century. The persistently weak AMOC, in concert with greenhouse gas reductions, leads to rapid cooling and sea ice growth in the subpolar North Atlantic. This cooling leads to a strong cyclonic atmospheric circulation anomaly over the North Atlantic subpolar gyre and, via atmospheric teleconnections, to the anticyclonic circulation anomaly over the Mediterranean. The failure to reverse the winter rainfall decline, despite substantial climate change mitigation, is an example of a "surprise" in the climate system. In this case, a persistent AMOC change unexpectedly impedes the reversibility of Mediterranean climate change. Such surprises could complicate pathways toward full climate recovery.
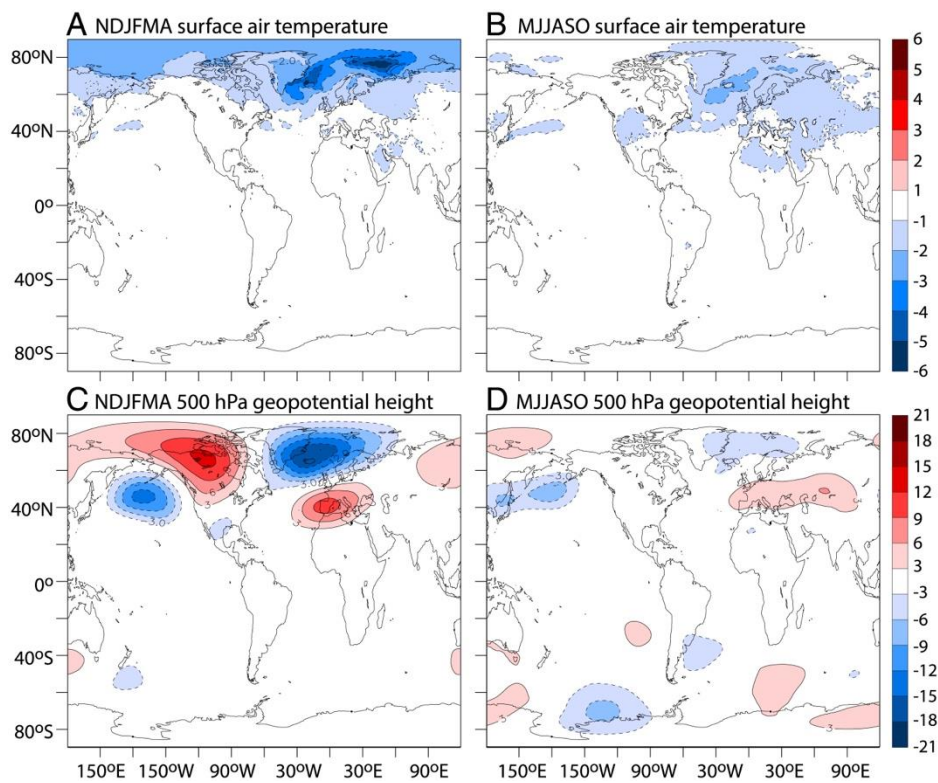
Figure 1. Differences for (A and B) surface air temperature and (C and D) 500 hPa geopotential

height for experiment SSP534OS. The differences are calculated as the mean over 2081 to 2100 minus the mean over 2046 to 2065. Units for temperature are °C and meters for 500 hPa geopotential height. For geopotential height the zonal mean was removed prior to plotting in order to accentuate regional structures. (A) Difference in surface air temperature for November to April (NDJFMA). (B) Same as A but for May to October (MJJASO). (C) Difference in 500 hPa geopotential height (NDJFMA). (D) Same as C but for MJJASO.
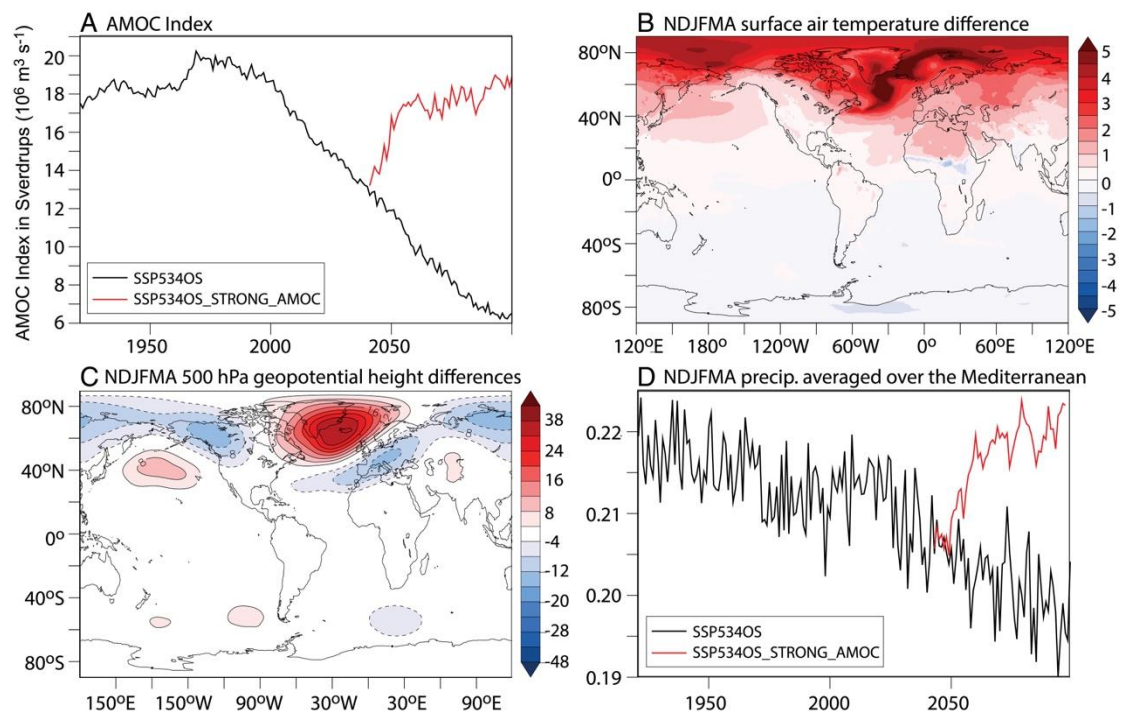
Figure 2. Results from an ensemble of simulations called "SSP534OS_STRONG_AMOC" (described in main text and in Mechanisms of the Persistent Mediterranean Winter Rainfall Decline). This tests the linkage between AMOC strength and the response of Mediterranean winter precipitation to greenhouse gas changes. (A) Indices of the AMOC at 45°N for SSP534OS (black) and SSP534OS_STRONG_AMOC (red). (B) Difference in winter (NDJFMA) surface air temperature for 2081 to 2100 for SSP534OS_STRONG_AMOC minus SSP534OS. Units are °C. (C) Same as B but for 500 hPa geopotential height. Units are meters. (D) Winter (NDJFMA) precipitation averaged over the Mediterranean for SSP534OS (black) and SSP534OS_STRONG_AMOC (red). Units are cm day^{-1}.

9. 北极海冰减少所诱发的 AMOC 减缓和恢复，以及持续的北大西洋暖洞

翻译人：张亚南 zhangyn3@mail.sustech.edu.cn

摘要：文中作者通过耦合环流模型（IPSL-CM5A2），研究了北极海冰减少对大西洋经向反转环流（AMOC）和北大西洋气候的影响，其中北极海冰减少直到达到夏季无冰的平衡。作者发现在几十年后由于冰岛表层海水的变暖引起的高密度下沉水团形成减少，从而导致 AMOC 的减弱；以及被随后的亚北极太平洋深水形成加强所弥补。因此，AMOC 在深层和高密度水域轻微减弱，而在较浅，密度较小的水域得到恢复。与此同时，风驱动的加强和亚极环流的东南向扩张导致 50°N 约 2°C 的冷异常在深度上的扩张，类似于大西洋"暖洞"。作者认为补偿的高密度水形成驱动了海冰退缩后 AMOC 的变化，"暖洞"的形成可以不依赖于 AMOC 的调节。

ABSTRACT: We investigate the impact of Arctic sea ice loss on the Atlantic meridional overturning circulation (AMOC) and North Atlantic climate in a coupled general circulation model (IPSL-CM5A2) perturbation experiment, wherein Arctic sea ice is reduced until reaching an equilibrium of an ice-free summer. After several decades we observe AMOC weakening caused by reduced dense water formation in the Iceland basin due to the warming of surface waters, and later compensated by intensification of dense water formation in the Western Subpolar North Atlantic. Consequently, AMOC slightly weakens in deep, dense waters but recovers through shallower, less dense waters overturning. In parallel, wind-driven intensification and southeastward expansion of the subpolar gyre cause a depth-extended cold anomaly ~2°C around 50°N that resembles the North

Atlantic "warming hole." We conclude that compensating dense water formations drive AMOC changes following sea ice retreat and that a warming hole can develop independently of the AMOC modulation.
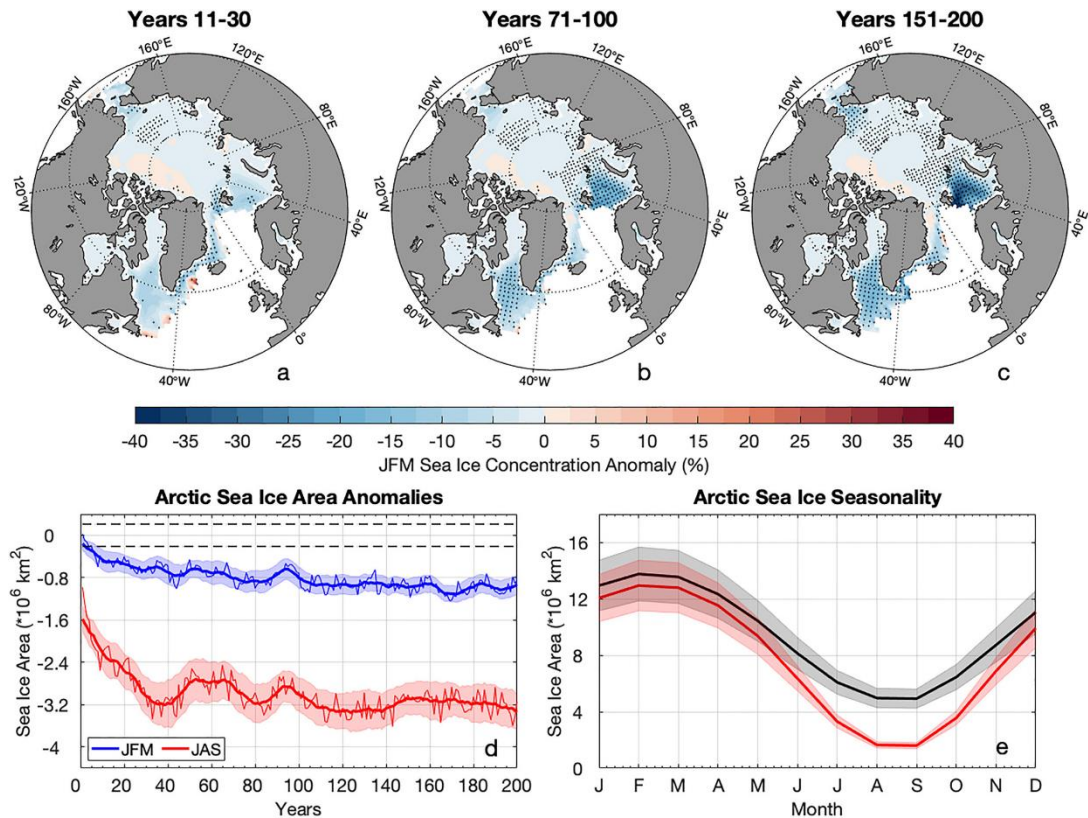
Figure 1. Ensemble mean of winter (JFM) sea ice anomalies for years (a) 11-30, (b) 71-100, and (c) 151-200 for the sea-ice perturbation experiment. Values with hatching are significant at a 95% confidence level. Induced changes in the total (d) Arctic sea ice area for winter (JFM, blue) and summer (JAS, red) and the (e) seasonality of the Arctic sea ice extent, taken for years 151-200 of the experiment. Thin and thick red lines in (c) indicate ensemble-mean and its 11-year running-mean, respectively; shading indicates ensemble spread to the 95% confidence threshold. For reference, the winter (summer) time-mean control sea ice area is $13.3 \pm 0.4 \times 106$ km2 ($5.3 \pm 0.5 \times 106$ km2). Summer (JAS) sea ice spatial anomalies are shown in Figure S1 in Supporting Information S1.
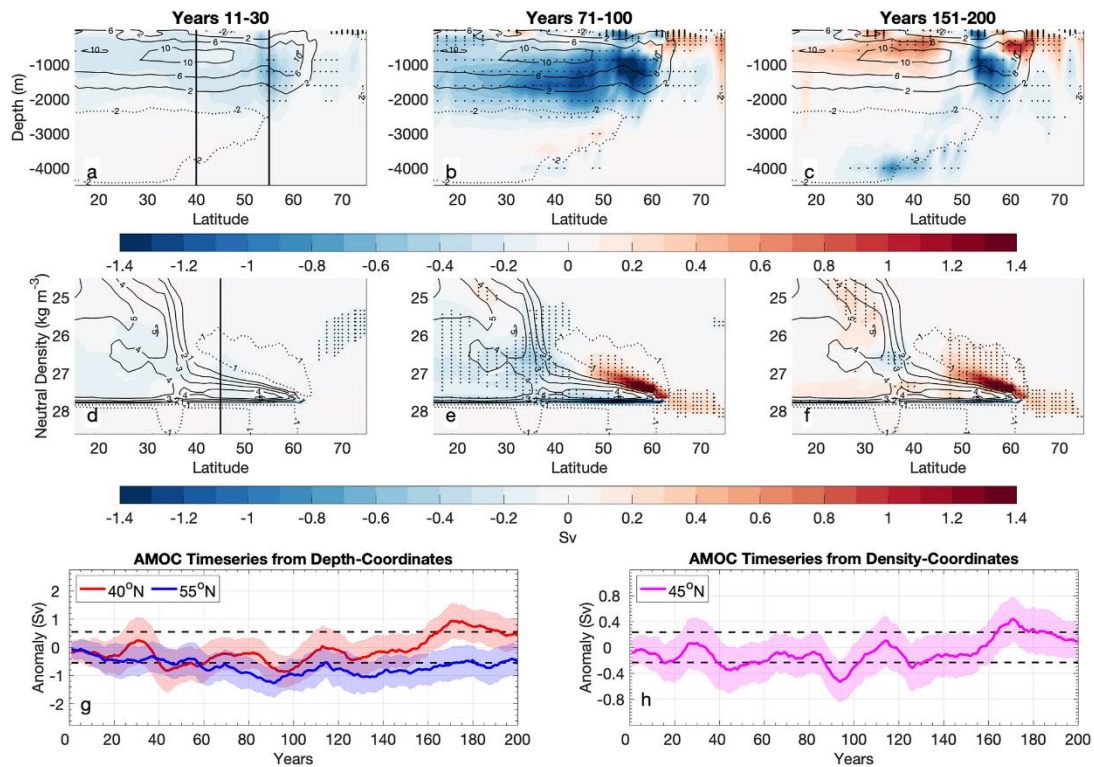
Figure 2. (a-c) Atlantic meridional overturning stream function in depth-coordinates for the control simulation (Sv, black contours) and its anomalies in the sea-ice perturbation experiments (color shading) for the same time intervals. (d-f) Atlantic meridional overturning stream function binned across neutral density coordinates (binned by 0.1 kg m^{-3}) in the control simulation (Sv, black contours) and its anomalies in the sea-ice perturbation experiments (color shading). Values with hatching are significant at a 95% confidence level. Timeseries of anomalous maximum AMOC (Sv) at (g) 40°N and 55°N from depth coordinates, similar to Simon et al. (2021), and (f) 45°N from density coordinates with an 11-year moving mean applied. The dashed black lines represent the 95% confidence interval of the control; shading indicates ensemble spread. The vertical black lines in (a,d) mark 40°N, 45°N, and 55°N-the latitudes used to evaluate AMOC strength in (g, h). The correlation of AMOC in depth and density space both at 40°N is ~0.90 and ~0.50 at 55°N in the control.
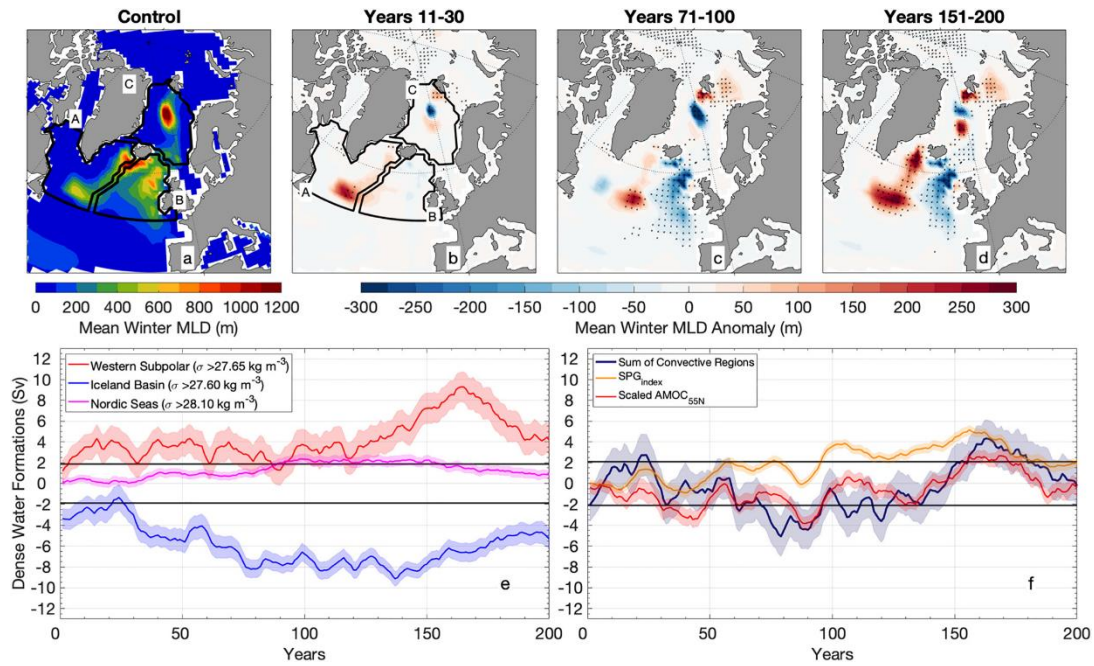
Figure 3. Mean winter (JFM) mixed layer depth (MLD) in (a) the control and (b-d) ensemble-mean anomalies in the sea-ice perturbation experiment for the same time intervals as in Figures 1 and 2. Three convective ocean basins are defined in (a) as the Labrador and Irminger Seas (a), Iceland basin (b), and Nordic Seas (c). (e-f) Ensemble-mean anomalous dense water formation rates in the perturbation experiment from a surface water mass transformation analysis; shading represents ensemble spread and an 11-year moving mean applied. Horizontal gray lines in (e-f) indicate the 95% confidence interval of the total dense water formation of the control. The entire North Atlantic convective region is represented in (f) as the sum of regions in (e). Note the large degree of compensation between changes in the (a) Labrador and Irminger Seas and the (b) Iceland Basin, which leads to AMOC decline followed by recovery. For comparison of the convective basins, the Subpolar Gyre index (SPG$_{index}$, absolute value of the minimum barotropic streamfunction) and a scaled AMOC$_{55N}$ index (AMOC$_{55N}$ timeseries from Figure 2h multiplied by 10) with an 11-year moving mean applied. At lag-zero, the AMOC$_{55N}$ (SPG$_{index}$) is correlated with the sum of the dense-water formation rates (DWF) at 0.72 (0.58), both significant at the 95% confidence level. The AMOC timeseries used is taken from density-coordinates.